Neural Network Detection for Bandwidth-Limited Non-Orthogonal Multiband CAP UVLC System

Jiang Chen, Zhe Wang, Yiheng Zhao, Junwen Zhang, Ziwei Li, Chao Shen, and Nan Chi

***Abstract*—In this paper, we propose a novel sparse data-to-symbol neural network (SDSNN) receiver for bandwidth-limited underwater visible light communication (UVLC) based on non-orthogonal multi-band carrierless amplitude and phase modulation (NM-CAP). Bandwidth limited NM-CAP signals usually carry severe inter-symbol interference (ISI) and inter-band interference (IBI). The SDSNN receiver directly converts the received NM-CAP data with ISI and IBI into quadrature amplitude modulation symbols without distortion for each sub-band. In contrast, the conventional receiver requires the least mean square (LMS) equalizer to cancel ISI, and the subcarrier component extraction with complex independent component analysis (SCE-ICA) to cancel IBI, respectively. SDSNN provides a novel receiving structure to replace post-equalization, matched filtering, and SCE-ICA. A blue-LED based UVLC system has been demonstrated utilizing NM-CAP16 with 3 sub-bands. The experimental results show that NM-CAP with the SDSNN receiver case reaches the highest spectral efficiency, where an enhancement of 43%, 20%, 6% has been measured over the orthogonal multi-band CAP case, NM-CAP with LMS equalizer case, and NM-CAP with joint LMS equalizer and SCE-ICA case, respectively. Compared with joint LMS equalizer and SCE-ICA case, the proposed SDSNN receiver can achieve 98% reduction of computational complexity.**

***Index Terms*—Non-orthogonal multi-band carrierless amplitude and phase, underwater visible light communication, neural network.**

I. Introduction

IN RECENT years, underwater application scenarios such as underwater vehicle surveillance, seabed geomorphology and seawater quality testing demand high-speed underwater wireless communication (UWC) technologies [1]–[3]. Although underwater acoustic communication technology is relatively mature, its low bandwidth leads to a limited transmission data rate. As for radio frequency, the power attenuation of radio in seawater limits its application in underwater communication [4]. Since blue and green light ($\lambda = 450 \sim 550$ nm) can transmit in water with relatively low attenuation, underwater visible light communication (UVLC) based on blue and green laser diodes (LDs) and light emitting diodes (LEDs) becomes a promising candidate for low-cost and high-speed UWC [1]–[5].

In general, the modulation bandwidth of LD is larger than that of LED. However, the divergence angle of LD is relatively small, so it requires strict alignment. In contrast, the LED has a larger divergence angle, which makes it useful in certain applications where alignment is difficult [3]. In a bandwidth limited UVLC system, spectrally efficient modulation formats, such as orthogonal frequency division multiplexing (OFDM) and carrierless amplitude and phase modulation (CAP) are widely used to reach high transmission data rate [6]. In [10], an OFDM modulation based underwater wireless optical communication system was demonstrated with data rate of 4.8 Gbps over 5.4-m transmission distance by employing a 450-nm TO-9 packaged and fiber-pigtailed LD. Unlike OFDM which utilizes inverse fast Fourier transform (IFFT) to modulate data in orthogonal sub-carriers, multi-band CAP (*m*-CAP) transmits data in sub-bands by orthogonal pulse shaping filters. Since the bandwidth allocation of *m*-CAP is flexible and the complexity is lower than OFDM, *m*-CAP is suitable for multi-user optical communication. In [11], an *m*-CAP based optical fiber communication scheme was designed for multiple users and experimentally demonstrated 11×5 sub-bands for 55 users with 9.3 Gbps per user with the help of wavelength division multiplexing. To achieve higher spectral efficiency (SE), a spectrally efficient frequency division multiplexing (SEFDM) proposed in [12] breaks the orthogonality of sub-carriers and employs overlapping of sub-carriers, comparing with the normal OFDM. Later, P. A. Haigh *et al.* proposed a non-orthogonal *m*-CAP (NM-CAP) based on modification of the subcarrier frequencies to force compression of adjacent sub-bands [13]. In [14], a multi-user NM-CAP VLC system was reported by adjusting the overlapping of each sub-band and allocating different bandwidths to each sub-band.

Owing to the non-orthogonality of NM-CAP, the overlapping in the adjacent sub-bands will lead to inter-band interference (IBI) per sub-band. IBI increases with the compression of bandwidth. To reduce IBI, a joint MIMO equalizer was proposed in a NM-CAP16 based indoor VLC system with 1.26-Gbps data rate [15]. Z. Wang *et al.* proposed a complex independent component analysis (ICA) algorithm based on subcarrier component extraction (SCE) to cancel IBI in the NM-CAP UVLC system for higher SE [16]. The experiment showed that the NM-CAP UVLC system based on SCE-ICA could improve the SE by as

Manuscript received December 16, 2021; revised February 28, 2022; accepted March 23, 2022. Date of publication March 25, 2022; date of current version April 14, 2022. This work was supported in part by the National Natural Science Foundation of China under Grants 61925104 and 62031011 and in part by the Natural Science Foundation of Shanghai under Grant 21ZR1406200. *(Corresponding authors: Chao Shen; Nan Chi.)*

The authors are with the Key Laboratory for Information Science of Electromagnetic Waves, Department of Communication Science and Engineering, Fudan University, Shanghai 200433, China (e-mail: 20210720083@fudan.edu.cn; 18110720075@fudan.edu.cn; zyh@fudan.edu.cn; junwenzhang@fudan.edu.cn; lizw@fudan.edu.cn; chaoshen@fudan.edu.cn; nanchi@fudan.edu.cn).

Digital Object Identifier 10.1109/JPHOT.2022.3162472

much as 40% compared with the non-compression M-CAP case. The main drawback of SCE-ICA is the weak ability of cancelling inter-symbol interference (ISI). As the bandwidth increases, the ISI caused by bandwidth limitation becomes severe, which will make SCE-ICA fail to compensate IBI due to the cumulative error effect. Thus, linear post-equalizers, such as a least mean square (LMS) based equalizer, is required to cancel ISI before using SCE-ICA. Moreover, due to the nonlinearity of VLC systems, deep neural network (DNN) equalizers are necessary for compensating nonlinearity [17], [18]. However, cascading post-equalizers and SCE-ICA will lead to high computational complexity. Thus, a new receiver with better performance and lower complexity is a critical topic in NM-CAP based systems.

In this paper, for the first time, we propose a sparse data-to-symbol neural network (SDSNN) receiver, which converts the received NM-CAP data with ISI and IBI to quadrature amplitude modulation (QAM) symbols without distortion of each sub-band, replacing the conventional receiver that is composed of post-equalization, matched filtering, and SCE-ICA. In a bandwidth limited VLC system based on NM-CAP, the SDSNN receiver can reach high SE with low computational complexity. We experimentally demonstrate a bandwidth-limited NM-CAP16 UVLC system based on a blue LED with 3 sub-bands. The experimental results show that the SDSNN receiver achieves the utmost SE enhancement of 43%, 20%, 6% compared with the orthogonal *m*-CAP case, NM-CAP with LMS equalizer case, and NM-CAP with joint LMS equalizer and SCE-ICA case, respectively. Moreover, by adopting the SDSNN receiver, the computational complexity can be reduced up to 98% compared with conventional NM-CAP receiver cascaded by LMS equalizer, matched filterers, and SCE-ICA.

II. Principles of NM-CAP and SDSNN Receiver

A. Principles of NM-CAP Modulation and Conventional NM-CAP Receiver

At the transmitter end, a set of *N* pseudorandom decimal binary sequences ranging from 0 to *M*−1 is generated, where *N* is the number of users, *M* is the order of QAM symbols. At the beginning of NM-CAP modulation, binary sequence is mapped to *M*-order complex QAM symbols according to Gray coding method, each of which carries log*M* bits. Then complex symbols are up-sampled according to the minimum number of samples per symbol (denoted by *S*) that will not lead to spectrum aliasing. Define $B = (1+\alpha)(1-\beta)$ as the normalized bandwidth, *S* can be given as $S = \lceil 2NB \rceil$, where $\lceil \cdot \rceil$ denotes the ceiling function, α denotes the roll-off factor of square root raised cosine (SRRC), β denotes the compression factor of the total bandwidth compared with non-overlapping *m*-CAP. The up-sampled signal is separated to in-phase (I) and quadrature (Q) and then passes through a pair of Hilbert pulse shaping filters, which are generated by multiplying SRRC filter and cosine waves and sine waves for I and Q, respectively[13]. The self-response filter of SRRC is raised cosine which satisfies the Nyquist criterion for zero ISI, so SRRC is used in a matched-filter-based CAP system. The center frequency of nth sub-band f_c^n can be given by:

$$f_c^n = \left[\frac{1}{2} + \frac{(n-1)[(1-\beta)N-1]}{N-1}\right](1+\alpha)R_{\mathrm{S}}, \quad n = 1, 2, \ldots, N \tag{1}$$

where R_{S} is the baud rate of each sub-band. (1) shows how to allocate frequency resources to each user. In particular, when $\beta = 0$, NM-CAP will turn into general orthogonal *m*-CAP without overlapping. The overlapping of adjacent sub-bands breaks the orthogonality between them. Thanks to the non-orthogonality of NM-CAP, the SE of the entire system is enhanced, which is expressed as:

$$\eta = \frac{\log(M)}{(1+\alpha)(1-\beta)}. \tag{2}$$

At the receiver end, due to the severe ISI caused by the limited bandwidth, the received waveform data must be equalized by an LMS equalizer, otherwise, the subsequent algorithm will become almost ineffective.

The recovered data passes through *N* pairs of matched filters, which are essentially bandpass filters at different center frequencies [17]. The matched filters length can be given by $L_{\mathrm{MF}} = SL + 1$, where *L* denotes the SRRC filter symbol length.

I and Q signal after matched filtering are combined to be complex signal, which is down-sampled to QAM symbols with severe IBI. The QAM symbols with IBI are recovered to symbols with weak IBI by SCE-ICA [16]. In SCE sub-algorithm, The QAM symbols with IBI are modulated to CAP signal by pulse shaping filters at different center frequencies. Then IBI components are extracted by adjacent matched filters. The QAM symbols with IBI and IBI components all pass through complex ICA to obtain clear QAM symbols.

B. Principle of SDSNN Based NM-CAP Receiver

Thanks to the universal approximation of an unknown mapping using a neural network [19], it is feasible to train a neural network model to convert received distorted NM-CAP data to clean QAM symbols without distortion, which can replace conventional post-equalization, matched filtering, and SCE-ICA.

The two demodulation schemes of NM-CAP with *N* sub-bands are shown in Fig. 1. Suppose we need to demodulate NM-CAP data *r*(*t*) to get *NK* QAM symbols $\mathbf{y}(k)$, where *K* denotes the symbol number of a sub-band that can be demodulated from the received data of *SK* length, where *t* = …, 0, 1, 2, …, *SK*−1, … and *k* = 0, 1, 2, *K*-1. $\mathbf{y}_k$ is expressed by:

$$\mathbf{y}(k) = \left[y_{\mathrm{I}}^1(k), y_{\mathrm{Q}}^1(k), y_{\mathrm{I}}^2(k), y_{\mathrm{Q}}^2(k), \ldots, y_{\mathrm{I}}^N(k), y_{\mathrm{Q}}^N(k)\right]^{\mathrm{T}} \tag{3}$$

where $y_{\mathrm{I}}^n(k)$ and $y_{\mathrm{Q}}^n(k)$ denote the I part and Q part of the QAM symbol of *n*th sub-band, respectively. In order to make *r*(*t*) and $\mathbf{y}(k)$ with one-to-one correspondence, the indices of *r*(*t*)

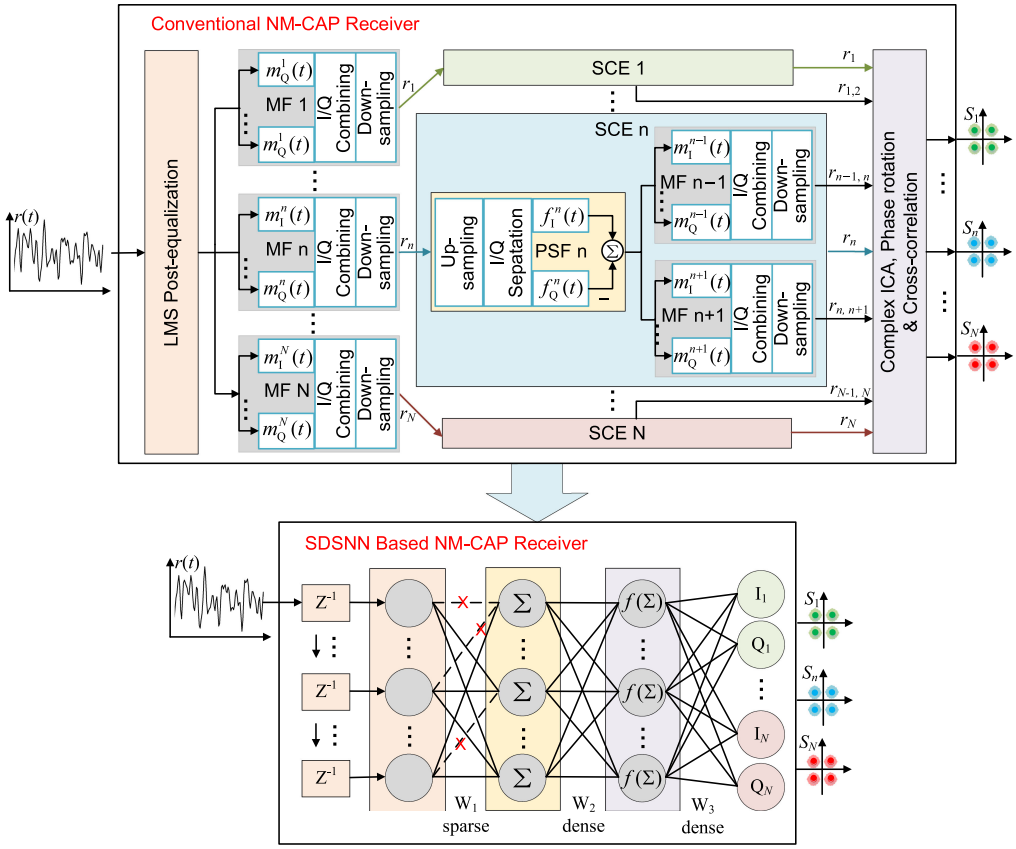

Fig. 1. The principle illustration of conventional NM-CAP receiver and SDSNN based NM-CAP receiver. MF: matched filter; PSF: pulse shaping filter; SCE: subcarrier component extraction.

are adjusted referring to $\mathbf{x}(k)$, which can be expressed by:

$$\mathbf{x}(k) = [r\left(Sk - L_{\text{in}}/2\right), r\left(Sk - L_{\text{in}}/2 + 1\right), \ldots, r(Sk), \ldots, r\left(Sk + L_{\text{in}}/2 - 1\right)]^{\text{T}} \quad (4)$$

where even number L_{in} is the input layer size of SDSNN. The size of rest layers is all $2N$, which means $\mathbf{W}_1$ is a L_{in}-by-$2N$ sparse matrix that can be pruned, $\mathbf{W}_2$ and $\mathbf{W}_3$ are both $2N$-by-$2N$ dense matrices that can't be pruned. $\mathbf{x}(k)$ passes through SDSNN to be $\mathbf{y}(k)$, thus the relationship between $\mathbf{x}(k)$ and $\mathbf{y}(k)$ is given by:

$$\mathbf{y}\left(k\right) = \mathbf{W}_3 f(\mathbf{W}_2(\mathbf{W}_1\mathbf{x}\left(k\right) + \mathbf{b}_1) + \mathbf{b}_2) + \mathbf{b}_3 \quad (5)$$

where $f(\cdot)$ denotes the nonlinear activation function (AF) $tanh(\cdot)$, $\mathbf{b}_1$, $\mathbf{b}_2$, and $\mathbf{b}_3$ are the bias of each layer. Because direct current (DC) in the received signal is nearly zero, bias $\mathbf{b}_1$, $\mathbf{b}_2$, and $\mathbf{b}_3$ are vectors with small values. In another word, in SDSNN model, bias can be treated as negligible.

For a data to symbol neural network (DSNN) without pruning, L_{in} should be larger than L_{MF}, which will be explained in the experimental results in Section IV. Considering computational complexity, $L_{\text{in}} = 3(L_{\text{MF}} - 1)/2$is suitable for the system. Because the tail of SRRC in time domain decays fast, L can be a small integer. The tail decays faster with the increase of roll-off factor. In the case of $\alpha = 0.2$, owing to slow decay of the tail, the power of SRRC filter disperses to its tail while the power of SRRC filter at $\alpha = 0.5$ converges in main pulse. For example, the normalized power of SRRC filter at $\alpha = 0.5$ achieves 0.999 within 4 symbol length while the case of $\alpha = 0.2$ achieves 0.999 within 8 symbol length. Moreover, thanks to the fast decay of the tail, ISI of CAP system based on SRRC filter at $\alpha = 0.5$ is lower than the case of $\alpha = 0.2$. Thus, Lin is lower in the case of $\alpha = 0.5$, which means the parameters of neural network is less, comparing with the case of $\alpha = 0.2$.

Different sub-bands need different information from $\mathbf{x}(k)$, thus, some weights of dense matrix $\mathbf{W}_1$ is redundant. To further reduce the computational complexity, it's necessary to prune the weights connected to input layer. Before pruning, the model with randomly initialized weights is trained for 20 epochs. After 20-epoch mini-batch training based on Adam optimizer [20], mean square error (MSE) is converged. Then 10% of the smallest active weights are pruned according to their absolute value. Weights that have been pruned are set to be inactive and can't be trained anymore. Pruning breaks the distribution of original weights, reduces active weights and increases inactive weights, so the pruned model must be retained for 5 epochs. After 5-epoch retraining, the model is pruned again. Repeat the above operations for N_{e} epochs, where Ne is the maximum number of epochs. In order to find the best count of pruning, the model is evaluated by its BER performance after retaining of each pruning.

C. Computational Complexity

Suppose the length of linear filter of LMS equalizer is L_{LMS}, then the computational complexity can be given by:

$$C_{\mathrm{LMS}} = SKL_{\mathrm{LMS}}. \tag{6}$$

Each subcarrier of NM-CAP needs 2 matched filters, so the count of matched filters is 2*N*, thus the count of multiplication in the process of matched filtering can be given by:

$$C_{\mathrm{MF}} = 2NSKL_{\mathrm{MF}}. \tag{7}$$

As mentioned above, different roll-off factor leads to different computational complexity. Roll-off factor should be selected according to the specific requirements for system. The count of pulse shaping is 2*N*. In the process of SCE, the count of additional matched filtering is 2(2*N*−2). Because pulse shaping and matched filtering are both linear convolution, the computational complexity of the SCE sub-algorithm can be expressed by:

$$C_{\mathrm{SCE}} = 2(3N-2)SKL_{\mathrm{MF}}. \tag{8}$$

The numerical complexity is given by [16]:

$$\begin{aligned} C_{\mathrm{ICA}} = {} & \min\left(KN_C^2/2 + 4N_C^3/3 + N_C^2K, 2KN_C^2\right) \\ & + N_C^3 + \left(16N_C^3/3 + N_C^2 + 3KN_C^2\right) iter \end{aligned} \tag{9}$$

where N_{C} denotes the number of mixing components with $N_{\mathrm{C}} = 3N-2$, and *iter* represents the number of iterations. The total computational complexity of matched filtering, LMS equalization and SCE-ICA algorithm is expressed by:

$$C_{\mathrm{Traditional}} = C_{\mathrm{LMS}} + C_{\mathrm{MF}} + C_{\mathrm{SCE}} + C_{\mathrm{ICA}}. \tag{10}$$

The computational complexity of SDSNN can be given by:

$$C_{\mathrm{SDSNN}} = 2(1-\delta)NKL_{\mathrm{in}} + 8KN^2 \tag{11}$$

where $\delta = 1-0.9m$ denotes the sparsity of SDSNN, *m* denotes the count of pruning. In general, $K >> N$, then we can get the following equation:

$$\frac{C_{\mathrm{SDSNN}}}{C_{\mathrm{Traditional}}} \approx \frac{\left[6(1-\delta)BL + 8\right]N^2}{(32N-16)N^2B^2L + 2NBL_{\mathrm{LMS}} + 3iter(3N-2)^2}. \tag{12}$$

It should be noted that the computational complexity of SDSNN is $\propto KLN^2$, while the computational complexity of MFs is $\propto KLN^3$. If a symbol based equalizer is used after MFs, the computational complexity will increase additionally. For example, the Viterbi maximum likelihood sequence estimator (MLSE) detector has a computational complexity $\propto KM^{l-1}$ [21], where *l* is the channel impulse response length, and *M* (=16) is the QAM order. The Viterbi MLSE detector is used to cancel ISI in symbol-based after matched filters and down-sampling. Therefore, the IBI caused by the overlapping of adjacent subbands will still remain by applying MLSE. Compared with MLSE, the proposed NN receiver can cancel ISI and IBI simultaneously. Another important feature of the NN receiver is that it can directly predict the symbols without passing through the matched filters. Hence the computational complexity for the NN receiver is much lower than that of the MLSE method.

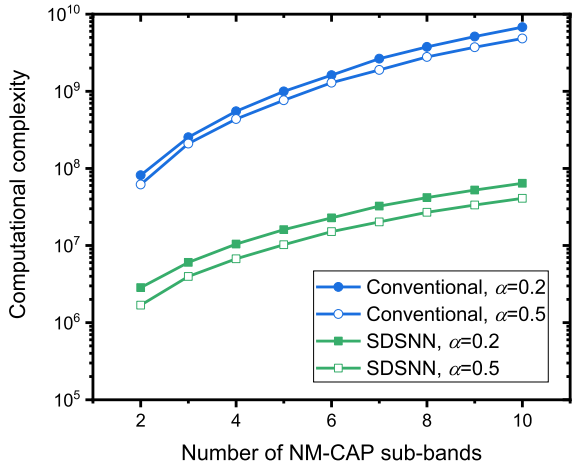

Fig. 2. The relationship between computational complexity and number of NM-CAP sub-bands.

Pruning is used to further reduce the complexity of the neural network. In fact, as shown in (12), even without pruning, the NN receiver reduces the system complexity significantly.

To show the specific numerical computational complexity, parameters in (12) are set according to the experimental results that will be described later in this paper. When $\alpha = 0.2$, we let $\beta = 0.1$, $L = 8$, $K = 2^{14}$, $\delta = 0.41$, $L_{\mathrm{LMS}} = 31$ and $iter = 50$. When $\alpha = 0.5$, we let $\beta = 0.2$, $L = 4$, $K = 2^{14}$, $\delta = 0.34$, $L_{\mathrm{LMS}} = 31$ and $iter = 50$. Based on those parameters, the relationship between computational complexity and number of NM-CAP sub-bands is plotted in Fig. 2. Computational complexity is a monotonic increasing function of number of subcarriers. At the same roll-off factor, the computational complexity of conventional algorithm is much higher than SDSNN. The computational complexity of $\alpha = 0.5$ case is lower than $\alpha = 0.2$ case in terms of the same algorithm. $C_{\mathrm{Traditional}}/C_{\mathrm{SDSNN}}$ becomes higher with the increase of *N*. When $N = 3$ and $\alpha = 0.5$, $C_{\mathrm{Traditional}}/C_{\mathrm{SDSNN}} = 42$, which means SDSNN achieves 97.6% reduction of computational complexity compared with conventional algorithm. When $N = 3$ and $\alpha = 0.2$, $C_{\mathrm{Traditional}}/C_{\mathrm{SDSNN}} = 53$, which means SDSNN achieves 98.1% reduction of computational complexity compared with conventional algorithm.

III. Experimental Setup

Fig. 3 presents the experimental setup of a 3-user UVLC system with the SDSNN receiver. At the transmitter end, each user's data is mapped to QAM16 complex symbols. Then the symbols are up-sampled at the count of 12, which is convenient to adjust different transmission bandwidths. Complex up-sampled symbols are separated to in-phase (I) and quadrature (Q) and then filtered by 3 pairs of pulse shaping filters, respectively. The real signals of 3 users are then summed as NM-CAP16 signal with 3 sub-bands. Sub-bands are numbered 1-3 in ascending order of frequency. Digital signal is converted to analog signal by an arbitrary wave generator (Tektronix AWG710B) at a sample frequency of 1.2 GSa/s. The generated analog signal is

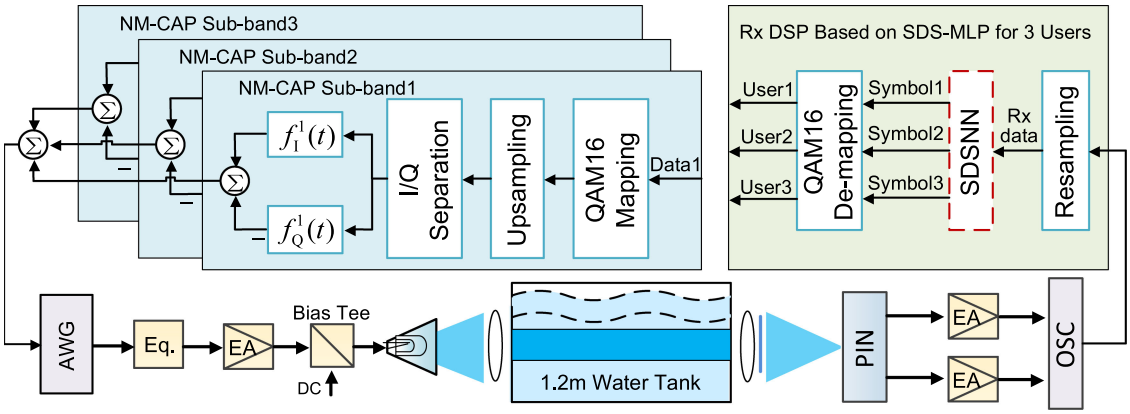

Fig. 3. The experimental setup of NM-CAP16 with 3 sub-bands UVLC system based on the SDSNN receiver.

pre-equalized by a circuit and amplified by an electrical amplifier (EA, Mini-Circuit ZHL-6A-S+) in sequence. Then the amplified signal is coupled with a direct current of 200 mA by a bias tee (Mini-Circuit ZFBT-4R2GW- FT+) to drive a blue silicon substrate LED of 17-MHz 3-dB modulation bandwidth. Blue light passes through a 1.2-m water tank filled with salted water. Note that the water is static and clean, which is suitable for blue light transmission with low attenuation. Since the distance of the VLC link is relatively short, the time jitter in the system is negligible even without timing recovery as long as the received data is synchronized well.

At the receiver end, blue light signal is detected by a PIN photodiode (Hamamatsu S10784), which converts the optical signal to electrical signal. The electrical signal passes through a pair of differential EAs and is sampled by an oscilloscope (Keysight DSO9404A) at the sampling frequency of 2 GSa/s in sequence. Then the received digital data is resampled to S samples per symbol which is expressed in Section II-A. After that the resampled NM-CAP16 data passes through SDSNN and is demodulated to 3 groups of QAM16 symbols for 3 users. At last, those QAM symbols are de-mapped to binary data. In order to prove that SDSNN has the function of post-equalization, matched filtering, and unmixing, conventional algorithm cascaded by LMS equalizer, matched filtering, and SCE-ICA is also used in the digital signal process (DSP) part. The size of the training dataset is 16384 groups of NM-CAP symbols, i.e., a total of 16384 sets of NM-CAP waveform vectors are used as the training dataset. The size of the test dataset is the same as that of the training dataset. Note that the random number generator of MATLAB of training dataset for SDSNN is different from that of the testing dataset, in order to avoid overfitting. The setting of dataset for LMS equalizer is the same as that of SDSNN. Moreover, the conventional algorithm only processes the testing data to calculate BER, in order to ensure the fairness of the comparison with SDSNN.

IV. Experimental Results

In this section, we first present the relationship of BER performance of the UVLC system and the sparsity of SDSNN. Here we let compression factor $\beta = 0.1$ when $\alpha = 0.2$, $\beta = 0.2$ when $\alpha = 0.5$. According to $S = \lceil 2NB \rceil$, sampling count S is 7 and 8 in $\alpha = 0.2$ and $\alpha = 0.5$ case, and matched filter length L_{MF} is 57 and 33, respectively. The baud rate of per sub-band is 100 Mbaud, which means the total baud rate of 3 sub-bands is 300 Mbaud. The peak-to-peak voltage (Vpp) is set as 1 V, where the nonlinearity is weak. 2^{16}-bit data per user is tested in the experiment, so the best BER of a sub-band is 1.5×10^{-5} and the best average BER of 3 sub-bands is 5×10^{-6}. Before training SDSNN models, we train DSNN models without pruning for 40 epochs. We first let $L_{\mathrm{in}} = L_{\mathrm{MF}} - 1$, the average BER is 4.58×10^{-5} and 1.07×10^{-4} in $\alpha = 0.2$ case and $\alpha = 0.5$ case, respectively. Then we let $L_{\mathrm{in}} = 1.5(L_{\mathrm{MF}} - 1)$, the average BER is 1.53×10^{-5} and 2.03×10^{-5} in $\alpha = 0.2$ case and $\alpha = 0.5$ case, respectively. The results illustrate that $L_{\mathrm{in}} = 1.5(L_{\mathrm{MF}} - 1)$ leads to good BER performance but higher complexity of neural network. The best way to reduce complexity is pruning.

Two SDSNN models in $\alpha = 0.2$ and $\alpha = 0.5$ cases are trained according to the training method mentioned in Section II. The training results are illustrated in Fig. 4. We firstly note that because of the pruning of the network, the MSE increased gradually after 20 epochs. We let $L_{\mathrm{in}} = 84$ in $\alpha = 0.2$ case and $L_{\mathrm{in}} = 48$ in $\alpha = 0.5$ case according to the above analysis. Note that the weights are pruned every 5 retraining epochs after 20 training epochs. In $\alpha = 0.2$ case, the lowest MSE is 0.0459 achieved at the epoch of 21, which is the first retraining epoch after the first pruning. The first pruning makes MSE reduce from 0.472 to 0.459, but later pruning all makes MSE increase. From the fourth pruning, increasing extent of MSE becomes larger. Although MSE changes, average BER keeps 1.53×10^{-5} before the sixth pruning. After the sixth pruning and corresponding 5-epoch retraining, BER increases from 1.53×10^{-5} to 5.09×10^{-5}. The results illustrate that SDSNN can tolerate 5 pruning, 0.41 sparsity for best BER performance. If the required BER is below 7% FEC limit of 3.8×10^{-3}, SDSNN can tolerate 17 pruning, 0.83 sparsity.

In the case of $\alpha = 0.5$, the lowest MSE is 0.0376 achieved at the epoch of 20, which is before the first pruning. Pruning makes MSE increase compared with $\alpha = 0.2$ case. From the third pruning, increasing extent of MSE becomes larger. Although MSE changes, average BER keeps 2.03×10^{-5} before the

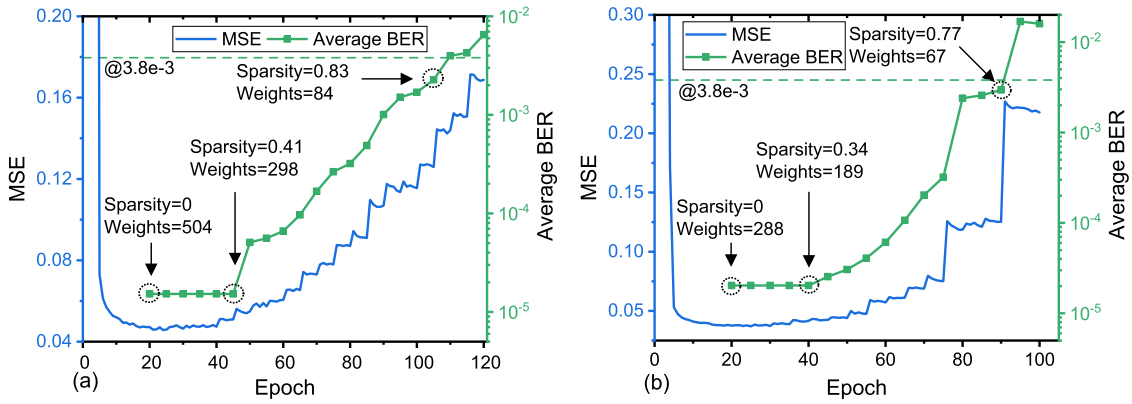

Fig. 4. Training results of SDSNN with different sparsity: (a) $\alpha = 0.2$, $\beta = 0.1$; (b) $\alpha = 0.5$, $\beta = 0.2$.

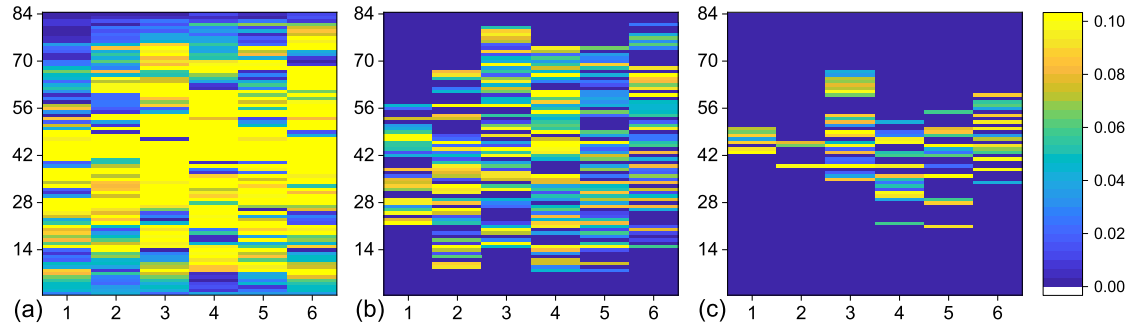

Fig. 5. Heat map of $\mathbf{W}_1$ in the case of $\alpha = 0.2$: (a) sparsity $= 0$, (b) sparsity $= 0.41$, and (c) sparsity $= 0.83$.

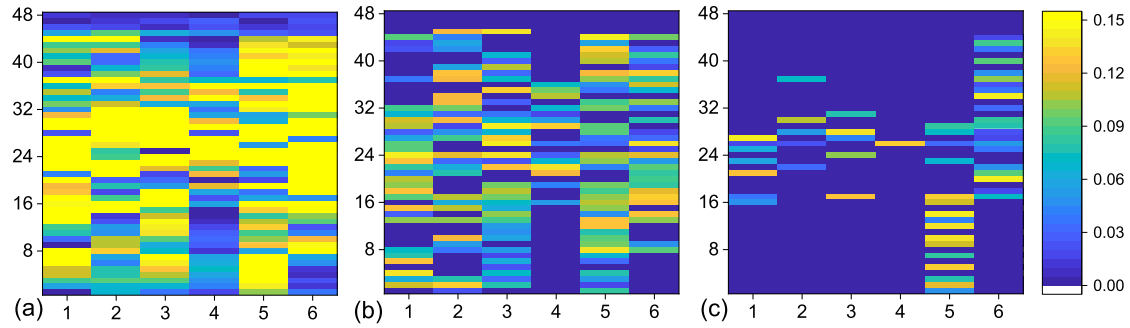

Fig. 6. Heat map of $\mathbf{W}_1$ in the case of $\alpha = 0.5$: (a) sparsity $= 0$, (b) sparsity $= 0.34$, and (c) sparsity $= 0.77$.

fifth pruning. After the fifth pruning and corresponding 5-epoch retraining, BER increases from 2.03×10^{-5} to 2.54×10^{-5}. The results illustrate that SDSNN can tolerate 4 pruning, 0.34 sparsity for best BER performance. If the required BER is below 7% FEC limit of 3.8×10^{-3}, SDSNN can tolerate 14 pruning, 0.77 sparsity.

Fig. 5 shows the weight distribution of $\mathbf{W}_1$ with different sparsity in the case of $\alpha = 0.2$. The x axis indicates 6 nodes of first hidden layer. The y axis indicates L_{in} nodes of the input layer. In another word, x axis and y axis indicate the column and the row of $\mathbf{W}_1$, respectively. When sparsity is 0, more than half of weights are greater than 0.08, and few weights are close to zero. When sparsity is 0.41, most of weights are below 0.08, and more than 41% weights are close to zero. When sparsity is 0.83, most weights are close to zero. Fig. 6 shows the weight distribution of $\mathbf{W}_1$ with different sparsity in the case of $\alpha = 0.5$. When sparsity is 0, more than half of weights are greater than 0.09, and few weights are close to zero. When sparsity is 0.34, most of weights are below 0.12, and more than 34% weights are close to zero. When sparsity is 0.77, most weights are close to zero. It's clear that most zero weights distribute on the edge of y axis, a few distribute in the middle.

Fig. 7 illustrates measured average BER as a function of Vpp. The total baud rate of 3 sub-bands is 300 MBaud. To show the nonlinearity of received signal, the amplitude magnitude (AM) response between transmitted data and received data after LMS

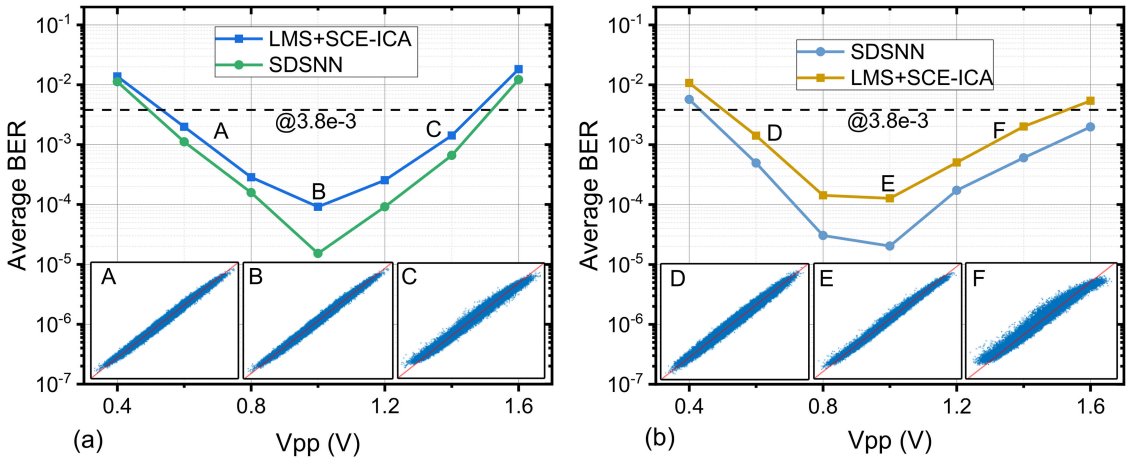

Fig. 7. The relationship between Vpp and the average BER: (a) $\alpha = 0.2$, $\beta = 0.1$; (b) $\alpha = 0.5$, $\beta = 0.2$.

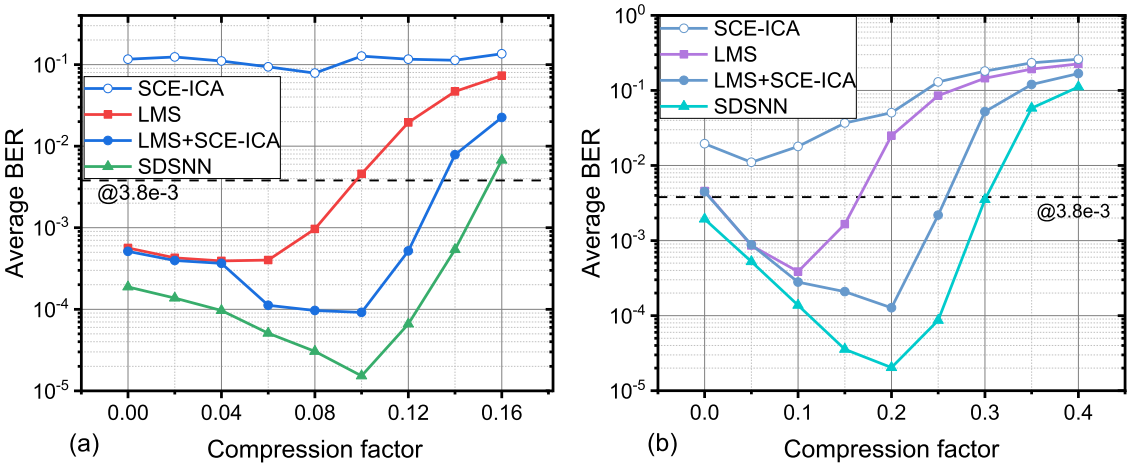

Fig. 8. The relationship between the spectral compression factor and the average BER: (a) $\alpha = 0.2$; (b) $\alpha = 0.5$.

linear equalizer is shown in the subfigures. Tested Vpp varies from 0.4 V to 1.6 V at 0.2 V increment, which is divided to 3 regions. In the first region where Vpp ranges from 0.4 V to 0.8 V, nonlinearity is weak. In this region, the main factor affecting BER is SNR, ISI, and IBI. The second Vpp region ranges from 0.8 V to 1.2 V, where nonlinearity is weak and SNR is higher. In this region, SDSNN offsets the weak nonlinearity, ISI and IBI. The third region ranges from 1.2 V to 1.6 V, where SNR is high enough but the BER performance is affected by the nonlinearity. In this region, nonlinearity mainly affects the first sub-band due to its highest power, IBI mainly affects the second sub-band due to the overlapping caused by two adjacent sub-bands, and ISI mainly affects the third sub-band due to the bandwidth limitation.

We let Vpp = 1 V where nonlinearity is weak and BER performance is the best to discuss IBI and ISI in this system. In $\alpha = 0.2$ case, the spectral compression factor β ranges from 0 to 0.16 while the compression factor in $\alpha = 0.5$ case ranges from 0 to 0.4. Fig. 8(a) and (b) show the relationship between the spectral compression factor and the average BER in $\alpha = 0.2$ case and $\alpha = 0.5$ case, respectively. In [16], the baud rate is 250 Mbaud and 200 Mbaud in $\alpha = 0.2$ case and $\alpha = 0.5$ case, respectively, the ISI generated by the bandwidth limitation is relatively weak, so a single SCE-ICA equalizer is able to achieve good performance. However, in this experiment of 300-Mbaud symbol rate, due to the severe ISI, a single SCE-ICA equalizer can hardly achieve expected performance. As shown in Fig. 8, the BER of the single SCE-ICA equalizer is all above 3.8×10^{-3}. In another word, SCE-ICA can hardly compensate IBI without an LMS equalizer.

In the case of $\alpha = 0.2$, when β varies from 0 to 0.04, ISI is dominant. Thanks to the compression, ISI caused by bandwidth limitation becomes weaker, which leads to the reduction of BER with the increment of β. SDSNN embodies the advantage of ISI equalization. When β varies from 0.04 to 0.10, IBI gradually becomes dominant as well as ISI. With the increment of β, BER of LMS equalizer case increases while BER of joint LMS equalizer and SCE-ICA case and SDSNN receiver case reduces, both of which reach the best BER performance at $\beta = 0.1$. When β varies from 0.10 to 0.16, IBI is more dominant than ISI, thus, BER in all cases increases with the increment of β. BER of LMS equalizer case reaches 3.8×10^{-3} at $\beta = 0.098$, where

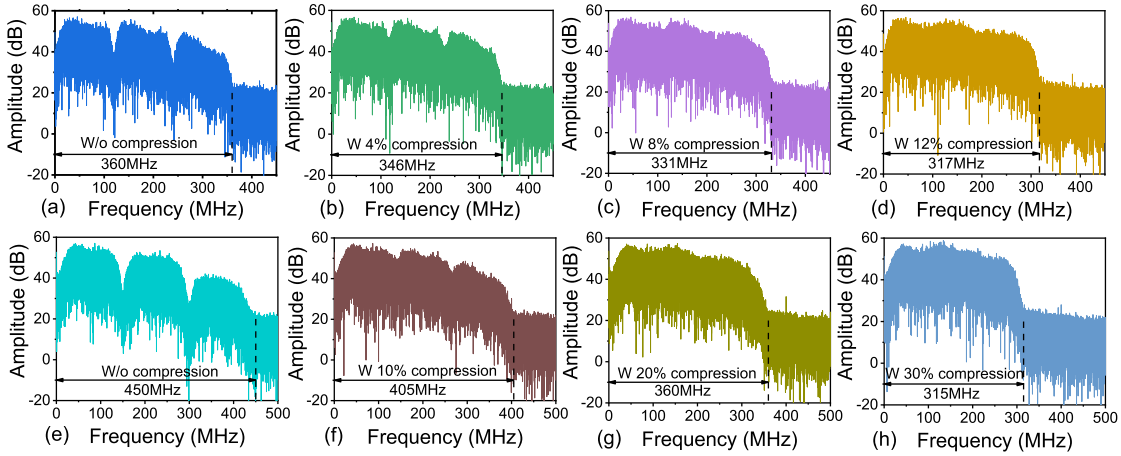

Fig. 9. The electrical spectrum of received signal: (a) $\alpha = 0.2$, $\beta = 0$; (b) $\alpha = 0.2$, $\beta = 0.04$; (c) $\alpha = 0.2$, $\beta = 0.08$; (d) $\alpha = 0.2$, $\beta = 0.12$; (e) $\alpha = 0.5$, $\beta = 0$; (f) $\alpha = 0.5$, $\beta = 0.1$; (g) $\alpha = 0.5$, $\beta = 0.2$; (h) $\alpha = 0.5$, $\beta = 0.3$.

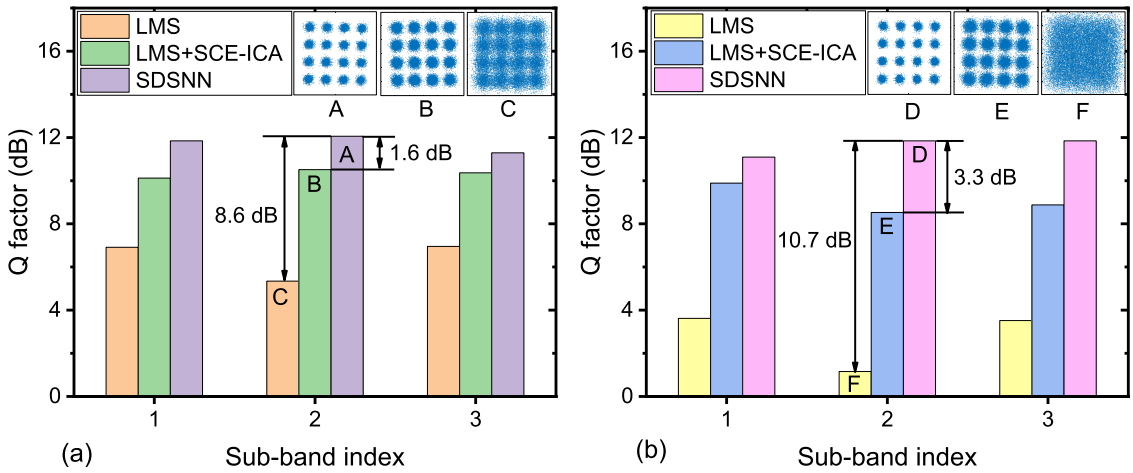

Fig. 10. The Q factor of each sub-band measured in different UVLC systems: (a) $\alpha = 0.2$, $\beta = 0.12$; (b) $\alpha = 0.\ 5$, $\beta = 0.25$.

$\eta = 3.70$ b/s/Hz. BER of joint LMS equalizer and SCE-ICA case reaches 3.8×10^{-3} at $\beta = 0.135$, where $\eta = 3.85$ b/s/Hz. BER of SDSNN receiver case reaches 3.8×10^{-3} at $\beta = 0.156$, where $\eta = 3.95$ b/s/Hz. NM-CAP with SDSNN case achieves the utmost SE enhancement of 19%, 7%, 3% compared with the orthogonal *m*-CAP case, NM-CAP with LMS equalizer case, and NM-CAP with joint LMS equalizer and SCE-ICA case, respectively.

In the case of $\alpha = 0.5$, when β varies from 0 to 0.1, ISI is dominant. Like $\alpha = 0.2$, ISI caused by bandwidth limitation becomes weaker thanks to the compression, which leads to the reduction of BER with the increment of β. SDSNN embodies the advantage of ISI equalization. When β varies from 0.1 to 0.2, IBI gradually becomes dominant as well as ISI. With the increment of β, BER of LMS equalizer case increases while BER of joint LMS equalizer and SCE-ICA case and SDSNN receiver case reduces, both of which reach the best BER performance at $\beta = 0.2$. When β varies from 0.2 to 0.4, IBI is more dominant than ISI, thus, BER in all cases increases with the increment of β. BER of LMS equalizer case reaches 3.8×10^{-3} at $\beta = 0.165$, where $\eta = 3.19$ b/s/Hz. BER of joint LMS and SCE-ICA case reaches 3.8×10^{-3} at $\beta = 0.259$, where $\eta = 3.60$ b/s/Hz. And BER of the SDSNN receiver case reaches 3.8×10^{-3} at $\beta = 0.301$, where $\eta = 3.82$ b/s/Hz. NM-CAP with SDSNN case achieves the utmost SE enhancement of 43%, 20%, 6% compared with the orthogonal *m*-CAP case, NM-CAP with LMS equalizer case, and NM-CAP with joint LMS equalizer and SCE-ICA case, respectively.

Fig. 9(a)∼(d) show the spectrum of received data in the $\alpha = 0.2$ case, where β ranges from 0 to 0.12, and bandwidth ranges from 317 MHz to 360 MHz. As shown in Fig. 10(a), the distortion of the third sub-band is most serious because the bandwidth is largest. As the compression of bandwidth increases, the spectrum distortion becomes less at the cost of overlapping in adjacent sub-bands. Fig. 9(e)∼Fig. 9(h) show the spectrum of received data in the $\alpha = 0.5$ case, where β ranges from 0 to 0.3, and bandwidth ranges from 315 MHz to 450 MHz. As shown in Fig. 10(e), the SNR of the third sub-band is lower owing to the larger bandwidth compared with the $\alpha = 0.2$ case. In addition, more compression is allowed in the $\alpha = 0.5$ case,

because the roll-off bandwidth is larger, which leads to less IBI, compared with the $\alpha = 0.2$ case.

In order to compare the different BER performances between each sub-band, the relationship between the sub-band index and the Q factor of each sub-band is investigated, as shown in Fig. 10. In the two cases, the Q factor of the second sub-band is lowest because of the overlapping by two adjacent sub-bands if only an LMS equalizer is used. When SCE-ICA or SDSNN are used, the Q factors of three sub-bands are increased sharply, proving that IBI is canceled by SCE-ICA and SDSNN. When $\alpha = 0.2$, $\beta = 0.12$, the highest enhancement of Q factor in SDSNN case is 8.6 dB and 1.6 dB compared with LMS equalizer case and joint LMS equalizer and SCE-ICA case, respectively. When $\alpha = 0.5$, $\beta = 0.25$, the highest enhancement of Q factor in SDSNN case is 10.7 dB and 3.3 dB compared with LMS equalizer case and joint LMS equalizer and SCE-ICA case, respectively.

V. Conclusion

In this paper, we propose and experimentally demonstrate the novel SDSNN receiver utilized in the bandwidth-limited NM-CAP UVLC system to cancel IBI caused by overlapping of adjacent sub-bands, ISI and nonlinear interference caused by the underwater channel. This novel receiver not only avoids the error accumulation effect caused by cascaded ISI equalizers, matched filters, and IBI equalizers; but also reduces the complexity of the system. The traditional algorithm using matched filters introduces additional IBI and the parameters of each equalizer are updated separately, which does not lead to a global optimum result.

In the experiment, we show that the proposed SDSNN receiver can achieve a better BER performance for every sub-band user. At the user level, the SDSNN receiver case shows a Q factor enhancement of 10.7 dB and 3.3 dB compared with the LMS equalizer case and the joint LMS equalizer and SCE-ICA case, respectively. At the system level, NM-CAP with SDSNN receiver case achieves SE enhancement of 43%, 20%, 6% compared with the orthogonal *m*-CAP case, NM-CAP with LMS equalizer case, and NM-CAP with joint LMS equalizer and SCE-ICA case, respectively. Moreover, thanks to the degenerate structure of the SDSNN receiver, a 98% reduction of computational complexity is achieved compared with the conventional receiver cascaded by LMS equalizer, matched filters, and SCE-ICA.

In our current work done in a lab testbed, the pruning-based learning can not only reduce the computational complexity but also achieve better performance. Due to the limitation of experimental conditions, we cannot conduct tests in a turbid underwater channel at present. But we believe the preliminary results indicate that the proposed new NN receiver is useful for an NM-CAP-based underwater VLC system.

References

[1] N. Chi, Y. Zhao, Y. Wei, and F. Hu, "Visible light communication in 6G: Advances, challenges, and prospects," *IEEE Veh. Technol. Mag.*, vol. 15, no. 4, pp. 93–102, Dec. 2020.

[2] Y. Zhao, P. Zou, W. Yu, and N. Chi, "Two tributaries heterogeneous neural network based channel emulator for underwater visible light communication systems," *Opt. Exp.*, vol. 27, no. 16, 2019, Art. no. 22532.

[3] H. Chen, J. Jia, W. Niu, Y. Zhao, and N. Chi, "Hybrid frequency domain aided temporal convolutional neural network with low network complexity utilized in UVLC system," *Opt. Exp.*, vol. 29, pp. 3296–3308, 2021.

[4] X. Liu *et al.*, "34.5 m underwater optical wireless communication with 2.70 Gbps data rate based on a green laser diode with NRZ-OOK modulation," *Opt. Exp.*, vol. 25, pp. 27937–27947, 2017.

[5] N. Chi, Y. Zhao, M. Shi, P. Zou, and X. Lu, "Gaussian kernel-aided deep neural network equalizer utilized in underwater PAM8 visible light communication system," *Opt. Exp.*, vol. 26, pp. 26700–26712, 2018.

[6] N. Chi and M. Shi, "Advanced modulation formats for underwater visible light communications," *Chin. Opt. Lett.*, vol. 16, 2018, Art. no. 120603.

[7] P. A. Haigh *et al.*, "A multi-CAP visible-light communications system with 4.85-b/s/Hz spectral efficiency," *IEEE J. Sel. Areas Commun.*, vol. 33, no. 9, pp. 1771–1779, Sep. 2015.

[8] F. M. Wu *et al.*, "Performance comparison of OFDM signal and CAP signal over high capacity RGB-LED-based WDM visible light communication," *IEEE Photon. J.*, vol. 5, no. 4, Aug. 2013, Art. no. 7901507.

[9] C. H. Yeh, H. Y. Chen, C. W. Chow, and Y. L. Liu, "Utilization of multi-band OFDM modulation to increase traffic rate of phosphor-LED wireless VLC," *Opt. Exp.*, vol. 23, no. 2, pp. 1133–1138, 2015.

[10] H. Oubei *et al.*, "4.8 Gbit/s 16-QAM-OFDM transmission based on compact 450-nm laser for underwater wireless optical communication," *Opt. Exp.*, vol. 23, pp. 23302–23309, 2015.

[11] J. Zhang, J. Yu, F. Li, N. Chi, Z. Dong, and X. Li, "11 × 5 × 9.3 Gb/s WDM-CAP-PON based on optical single-side band multi-level multi-band carrier-less amplitude and phase modulation with direct detection," *Opt. Exp.*, vol. 21, pp. 18842–18848, 2013.

[12] I. Darwazeh, T. Xu, T. Gui, Y. Bao, and Z. Li, "Optical SEFDM system; bandwidth saving using non-orthogonal sub-carriers," *IEEE Photon. Technol. Lett.*, vol. 26, no. 4, pp. 352–355, Feb. 2014.

[13] P. A. Haigh, P. Chvojka, Z. Ghassemlooy, S. Zvanovec, and I. Darwazeh, "Non-orthogonal multi-band CAP for highly spectrally efficient VLC systems," in *Proc. 11th Int. Symp. Commun. Syst., Netw. Digit. Signal Process.*, 2018, pp. 1–6.

[14] P. Pešek, P. A. Haigh, O. I. Younus, P. Chvojka, Z. Ghassemlooy, and S. Zvánovec, "Experimental multi-user VLC system using non-orthogonal multi-band CAP modulation," *Opt. Exp.*, vol. 28, pp. 18241–18250, 2020.

[15] S. Liang, L. Qiao, X. Lu, and N. Chi, "Enhanced performance of a multiband super-Nyquist CAP16 VLC system employing a joint MIMO equalizer," *Opt. Exp.*, vol. 26, pp. 15718–15725, 2018.

[16] Z. Wang, J. Chen, and N. Chi, "A novel algorithm for improving the spectrum efficiency of non-orthogonal multiband CAP UVLC systems," *J. Lightw. Technol.*, vol. 38, pp. 6187–6201, 2020.

[17] J. Chen and N. Chi, "Pulse shapings employed in an underwater visible-light communication system based on carrierless amplitude and phase modulation utilizing a complex deep neural network equalizer," *Opt. Eng.*, vol. 59, no. 10, 2020, Art. no. 106110.

[18] Y. Zhao and N. Chi, "Partial pruning strategy for a dual-branch neural network-based post-equalizer in underwater visible light communication systems," *Opt. Exp.*, vol. 28, pp. 15562–15572, 2020.

[19] K. Hornik, M. Stinchcombe, and H. White, "Universal approximation of an unknown mapping and its derivatives using multilayer feedforward networks," *Neural Netw.*, vol. 3, no. 5, pp. 551–560, 1990.

[20] D. P. Kingma and J. L. Ba, "Adam: A method for stochastic optimization," in *Proc. 3rd Int. Conf. Learn. Represent.*, 2015, pp. 1–15.

[21] H. C. Myburgh and J. C. Olivier, "Near-Optimal low complexity MLSE equalization," in *Proc. IEEE Wireless Commun. Netw. Conf.*, 2008, pp. 226–230.